AFRL-AFOSR-JP-TR-2024-0044

Data driven approaches for unsteady flow control over dynamically stalling wings

SRIDHAR RAVI
UNIVERSITY OF NEW SOUTH WALES
HIGH ST
KENSINGTON, , 2052
AUS

01/23/2024
Final Technical Report

Air Force Research Laboratory
Air Force Office of Scientific Research
Asian Office of Aerospace Research and Development
Unit 45002, APO AP 96338-5002

REPORT DOCUMENTATION PAGE

PLEASE DO NOT RETURN YOUR FORM TO THE ABOVE ORGANIZATION.

1. REPORT DATE	2. REPORT TYPE	3. DATES COVERED	
20240123	Final	START DATE 20220708	END DATE 20230707

4. TITLE AND SUBTITLE
Data driven approaches for unsteady flow control over dynamically stalling wings

5a. CONTRACT NUMBER	5b. GRANT NUMBER	5c. PROGRAM ELEMENT NUMBER
	FA2386-22-1-4036	61102F
5d. PROJECT NUMBER	**5e. TASK NUMBER**	**5f. WORK UNIT NUMBER**

6. AUTHOR(S)
Sridhar Ravi, Sunetra Sarkar, Fangbao Tian, John Young

7. PERFORMING ORGANIZATION NAME(S) AND ADDRESS(ES)
UNIVERSITY OF NEW SOUTH WALES
HIGH ST
KENSINGTON 2052
AUS

8. PERFORMING ORGANIZATION REPORT NUMBER

9. SPONSORING/MONITORING AGENCY NAME(S) AND ADDRESS(ES)	10. SPONSOR/MONITOR'S ACRONYM(S)	11. SPONSOR/MONITOR'S REPORT NUMBER(S)
AOARD UNIT 45002 APO AP 96338-5002	AFRL/AFOSR IOA	AFRL-AFOSR-JP-TR-2024-0044

12. DISTRIBUTION/AVAILABILITY STATEMENT
A Distribution Unlimited: PB Public Release

13. SUPPLEMENTARY NOTES

14. ABSTRACT
This project is aiming at two subjects for investigating the passive flapping motion of wings at low Reynolds numbers and for computational method on dynamic mode decomposition for unsteady flow over flapping wings.
For the passive flapping motion, PI proposed a fluid-structure interaction (FSI) model that couples two elastic wing-hinge dynamics and unsteady flapping aerodynamics to explore passive flapping and pitching mechanisms in a fruit-fly model. A fruit fly wing in hover with prescribed flapping and passive pitching was performed to validate the proposed two elastic wing-hinge model. A passive flapping and pitching wing simulation was performed based on the validated model. The computational results of the passive pitching motion are in good agreements over a phase of fifty degree.
For unsteady flow over flapping wings, dynamic mode decomposition (DMD) has attracted growing interest in the research community due to recent advancements in generating large experimental and numerical data sets. An in-house code based on the immersed boundary-lattice Boltzmann method (IB-LBM) was used for the flow simulations on dynamically oscillating wings. An in-house MATLAB code of DMD was successfully used to analyze the wake and the unsteady separation of boundary layers at the leading edge. This method can provide snapshots of the flow field and computes the modes that govern the dynamics. Good agreement of results between current computations and published data was observed, suggesting the present FSI solver can accurately compute the flow over flapping wing systems.

15. SUBJECT TERMS

16. SECURITY CLASSIFICATION OF:			17. LIMITATION OF ABSTRACT	18. NUMBER OF PAGES
a. REPORT	b. ABSTRACT	c. THIS PAGE		
U	U	U	SAR	23

19a. NAME OF RESPONSIBLE PERSON	19b. PHONE NUMBER *(Include area code)*
FUMIO KOJIMA	315-227-7007

Standard Form 298 (Rev.5/2020)
Prescribed by ANSI Std. Z39.18

Data-driven approaches for unsteady flow control over dynamically stalling wings

Name and Position/Title of Principle Investigator:
Dr Sridhar Ravi, Associate Professor, UNSW-Canberra

Key Researcher(s) involved in the Proposed Project:
Dr Qiuxiang Huang, Research Associate, UNSW-Canberra
Dr Shantanu Bhat, Research Associate, UNSW-Canberra

Contents

1 Investigation of the passive flapping motion of wings at low Reynolds numbers

1.1 Introduction

Many insects have spring-like elements in the form of elastic materials in their thoraxes, muscles, and tendons that may reduce the energetic demands of flapping flight and improve flight efficiency Lynch et al. (2021). Their flight mechanisms have been studied extensively by researchers worldwide through direct kinematics measurements (Bergou et al., 2007; Chen et al., 2019), numerical (Bergou et al., 2007; Chen et al., 2016; Huang et al., 2023) and analytical modelling (Ennos, 1988; Whitney and Wood, 2010). Recent progress was reviewed by Shyy et al. (2016) and Eldredge and Jones (2019). Insects can be generally divided into two groups based on flight mechanisms. The first group is insects with direct-flight actuation, such as dragonflies and mayflies, whose flight muscles insert directly into the hinged base of their wings and cause the wings to flap by initiating movements in the base. The other group is the insects with indirect-flight actuation, such as bumblebees and butterflies, whose flight muscles attach to the walls of their thorax instead of the wings. The muscle contractions distort the thorax shape, which in turn causes the wings to move since the wings are extensions of the thoracic exoskeleton. Direct-flight actuation has been widely studied (Spagnolie et al., 2010; Chen et al., 2016; Huang et al., 2021a, 2023), while flight via indirect actuation remains poorly explored. In this study, we propose a fluid-structure interaction (FSI) model that couples two elastic wing-hinge dynamics and unsteady flapping aerodynamics to explore passive flapping and pitching mechanisms in a fruit-fly model. This study may enable us to fill the important knowledge gaps by reaching new levels of understanding of insects' actuation mechanism of indirect-flight muscles.

1.2 Model description

The unsteady incompressible flow is governed by the continuity and Navier-Stokes equations

$$\nabla \cdot \boldsymbol{u} = 0, \quad \frac{\partial \boldsymbol{u}}{\partial t} + \boldsymbol{u} \cdot \nabla \boldsymbol{u} = -\frac{1}{\rho}\nabla p + \nu \nabla^2 \boldsymbol{u} + \boldsymbol{f}, \tag{1}$$

where $\boldsymbol{u}$ is the fluid velocity, ρ is the constant density, $\boldsymbol{f}$ is the body force and p and ν are pressure and kinematic viscosity, respectively.

1.3 Derivation of the passively pitching and flapping wing kinematics

Schematic diagram in figure 1 shows the definitions of a rectangular wing planform. The wing was assumed as a thin (ignore the thickness) and rigid plate for simplified analysis. In this model, the two angles of concern are the the stroke position angle ϕ around $Z-$axis and the pitching angle θ around the torsion axis (i.e., pitching axis). Here, the pitching axis was aligned with the leading edge of the wing.

From Newton's second law of motion in classical mechanics, the total torque $\tilde{T}$ applied on the wing root to actuate the flapping-wing system equals to the rate of change of angular

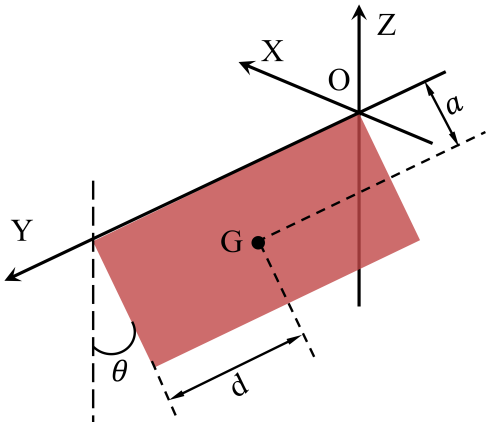

Figure 1: Coordinates and dimensions for a rectangular wing planform: G is the centre of mass and θ is the pitching angle. $Z-$axis and $Y-$axis are the flapping axis and pitching axis, respectively. The wing has a chord length $2a$ and a span of $2d$.

momentum $\tilde{H}$, i.e.,

$$\tilde{T} = \frac{d}{dt}(\tilde{H}). \tag{2}$$

The flapping-wing system is then decomposed into pitching and flapping motions, as shown in figures 2 and 3.

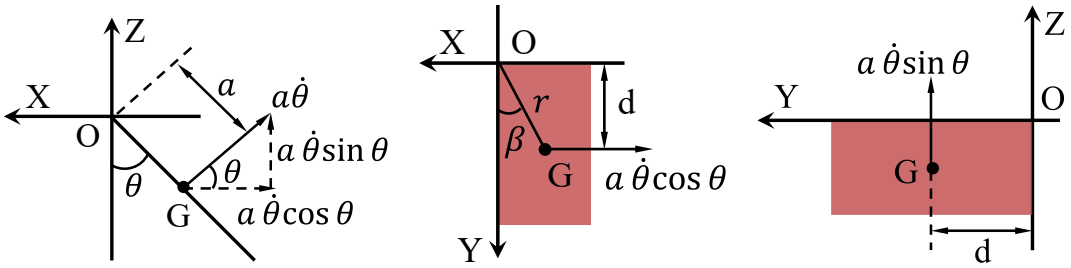

(a) $X-Z$ plane; (b) $X-Y$ plane; (c) $Y-Z$ plane

Figure 2: Pitching motion analysis in three different views. $a\dot{\theta}$ is the tangential pitching velocity at the centre of mass G.

For the pitching, the angular momentum is $\tilde{H}_{pitch} = \overline{r} \times m\overline{v}$, where $\overline{r} = (\hat{u}_x, \hat{u}_y, \hat{u}_z)$ is the position vector of the centre of mass (relative to the wing root), $m = 4\rho_w ad$ is the wing mass, ρ_w is the wing density, and $\overline{v}$ is the linear velocity vector at G. According to the resolved motions in three different views in figure 2, the pitching angular momentum $\tilde{H}_p$ is more specifically calculated as

$$\tilde{H}_{pitch} = ma\dot{\theta} \cdot a\hat{u}_y + ma\dot{\theta}\cos\theta \cdot d\hat{u}_z + ma\dot{\theta}\sin\theta \cdot d\hat{u}_x. \tag{3}$$

For the flapping motion, as shown in figure 3, the radius of rotation or the length of the moment arm r and it's angle definitions can be calculated as

$$r = \sqrt{d^2 + a^2\sin^2\theta}, \quad \cos\beta = \frac{d}{r}, \quad \sin\beta = \frac{a\sin\theta}{r}. \tag{4}$$

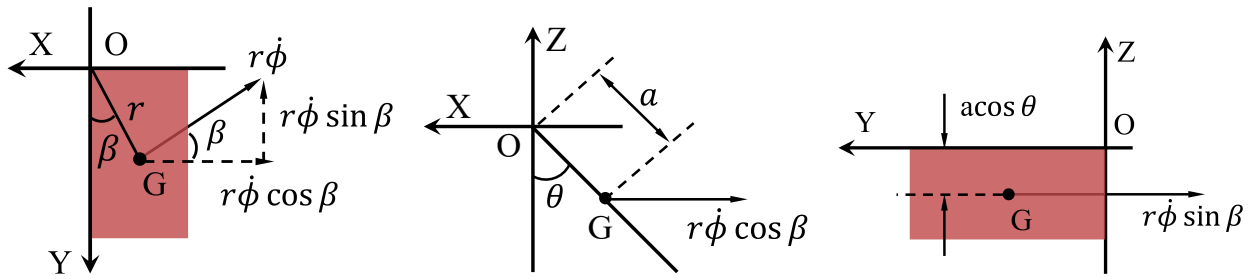

(a) $X-Y$ plane; (b) $X-Z$ plane; (c) $Y-Z$ plane.

Figure 3: Flapping motion analysis in three different views. $r\dot{\phi}$ is the tangential flapping velocity at the centre of mass G.

Similarly, according to the resolved motions in three different views, the flapping angular momentum $\tilde{H}_{flap}$ can be calculated as

$$\tilde{H}_{flap} = mr\dot{\phi}\cdot r\hat{u}_z + mr\dot{\phi}\cos\beta\cdot a\cos\theta\hat{u}_y - mr\dot{\phi}\sin\beta\cdot a\cos\theta\hat{u}_x \tag{5}$$

Therefore, the total momentum $\tilde{H}$ of the flapping-wing system is

$$\begin{aligned}\tilde{H} &= \tilde{H}_{pitch} + \tilde{H}_{flap}\\ &= (ma^2\dot{\theta} + mad\dot{\phi}\cos\theta)\hat{u}_y + (mad\dot{\theta}\sin\theta - ma^2\sin\theta\cos\theta\dot{\phi})\hat{u}_x + (mad\dot{\theta}\cos\theta + mr^2\dot{\phi})\hat{u}_z.\end{aligned} \tag{6}$$

For a general (non-rectangular) wing, we define the wing in the non-pitched position with subscript o (i.e., $\theta = 0$ and $x = 0$). Then, the moment of inertia around the flapping axis ($Z-$axis) when the wing is rotated around the pitching axis J_{yzo} is calculated as

$$J_{yzo} = -\int yzdm = -\rho_w\int_{-2a}^{0}\int_{0}^{2d} yzdydz = -4\rho_w adad = -mad. \tag{7}$$

Similarly, the moment of inertia around the pitching axis J_{yyo} and the moment of inertia around the flapping axis J_{zzo} are, respectively, given as

$$J_{yyo} = \int(x^2+z^2)dm = \frac{1}{3}m(2a)^2, \quad J_{zzo} = \int(x^2+y^2)dm = \frac{1}{3}m(2d)^2. \tag{8}$$

Substituting equations 7 and 8 into equation 6, this gives

$$\begin{aligned}\tilde{H} = &\underbrace{(J_{yyo}\dot{\theta} - J_{yzo}\dot{\phi}\cos\theta)\hat{u}_y}_{pitch} + \underbrace{(-J_{yzo}\dot{\theta}\sin\theta - \frac{1}{2}J_{yyo}\dot{\phi}\sin 2\theta)\hat{u}_x}_{roll}\\ &+ \underbrace{\left[-J_{yzo}\dot{\theta}\cos\theta + (J_{zzo} + J_{yyo}\sin^2\theta)\dot{\phi}\right]\hat{u}_z}_{flap}.\end{aligned} \tag{9}$$

If the deviation angle outside the stroke plane is taken as zero, then

$$\frac{d}{dt}(\hat{u}_z) = 0. \tag{10}$$

In addition, the Cartesian coordinate system ($\hat{u}_x$, $\hat{u}_y$, $\hat{u}_z$) and the cylindrical coordinate system ($\hat{u}_\phi$, $\hat{u}_r$, $\hat{u}_z$) have the following relationships

$$\begin{aligned} \hat{u}_x &= -\hat{u}_\phi, \quad \frac{d}{dt}\left(\hat{u}_x\right) = -\frac{d}{dt}\left(\hat{u}_\phi\right) = \dot{\phi}\hat{u}_r = \dot{\phi}\hat{u}_y, \\ \hat{u}_y &= \hat{u}_r, \quad \frac{d}{dt}\left(\hat{u}_y\right) = \frac{d}{dt}\left(\hat{u}_r\right) = \dot{\phi}\hat{u}_\phi = -\dot{\phi}\hat{u}_x. \end{aligned} \tag{11}$$

Then, the total torque $\tilde{T}$ applied on the wing root can be calculated as

$$\begin{aligned} \tilde{T} = \frac{d\tilde{H}}{dt} &= \left(J_{yyo}\ddot{\theta} - J_{yzo}\ddot{\phi}\cos\theta + J_{yzo}\dot{\phi}\dot{\theta}\sin\theta\right)\hat{u}_y \\ &\quad - \left(J_{yyo}\dot{\theta} - J_{yzo}\dot{\phi}\cos\theta\right)\dot{\phi}\hat{u}_x \\ &\quad + \left(-J_{yzo}\ddot{\theta}\sin\theta + J_{yzo}\dot{\theta}^2\cos\theta - \frac{1}{2}J_{yyo}\ddot{\phi}\sin 2\theta - J_{yyo}\dot{\phi}\dot{\theta}\cos 2\theta\right)\hat{u}_x \\ &\quad + \left(-J_{yzo}\dot{\theta}\sin\theta - \frac{1}{2}J_{yyo}\dot{\phi}\sin 2\theta\right)\dot{\phi}\hat{u}_y \\ &\quad + \left(-J_{yzo}\ddot{\theta}\cos\theta + J_{yzo}\dot{\theta}^2\sin\theta + J_{zzo}\ddot{\phi} + J_{yyo}\sin^2\theta\ddot{\phi} + J_{yyo}\sin 2\theta\dot{\phi}\dot{\theta}\right)\hat{u}_z. \end{aligned} \tag{12}$$

Reorganise equation 12 and this gives

$$\begin{aligned} \tilde{T} = &\underbrace{\left[-\left(J_{yyo}\dot{\theta} - J_{yzo}\dot{\phi}\cos\theta\right)\dot{\phi} + \left(-J_{yzo}\ddot{\theta}\sin\theta + J_{yzo}\dot{\theta}^2\cos\theta - \frac{1}{2}J_{yyo}\ddot{\phi}\sin 2\theta - J_{yyo}\dot{\phi}\dot{\theta}\cos 2\theta\right)\right]}_{roll}\hat{u}_x \\ &+ \underbrace{\left(J_{yyo}\ddot{\theta} - J_{yzo}\ddot{\phi}\cos\theta - \frac{1}{2}J_{yyo}\dot{\phi}^2\sin 2\theta\right)}_{pitch}\hat{u}_y \\ &+ \underbrace{\left(J_{zzo}\ddot{\phi} + J_{yyo}\sin^2\theta\ddot{\phi} - J_{yzo}\ddot{\theta}\cos\theta + J_{yzo}\dot{\theta}^2\sin\theta + J_{yyo}\sin 2\theta\dot{\phi}\dot{\theta}\right)}_{flap}\hat{u}_z. \end{aligned} \tag{13}$$

Then, the flapping and pitching inertial torque are

$$\begin{aligned} T_{iner}^{flap} &= \left(J_{zzo} + J_{yyo}\sin^2\theta\right)\ddot{\phi} + J_{yyo}\sin(2\theta)\dot{\theta}\dot{\phi} - J_{yzo}\left(\ddot{\theta}\cos\theta - \dot{\theta}^2\sin\theta\right), \\ T_{iner}^{pitch} &= J_{yyo}\ddot{\theta} - J_{yzo}\ddot{\phi}cos\theta - \frac{1}{2}J_{yyo}\dot{\phi}^2 sin2\theta. \end{aligned} \tag{14}$$

Therefore, for the fully prescribed motions the total input torque to actuate the wing flap and pitch can be calculated, respectively, as

$$\begin{aligned} T_{\text{Input}}^{flap} &= \underbrace{\left(J_{zz} + J_{yy}\sin^2\theta\right)\ddot{\phi} + J_{yy}\sin(2\theta)\dot{\theta}\dot{\phi} - J_{yz}\left(\ddot{\theta}\cos\theta - \dot{\theta}^2\sin\theta\right)}_{T_{iner}^{flap}} - T_{aero}^{flap}, \\ T_{\text{Input}}^{pitch} &= \underbrace{-J_{yy}\ddot{\theta} + J_{zy}\ddot{\phi}cos\theta + \frac{1}{2}J_{yy}\dot{\phi}^2 sin2\theta}_{T_{iner}^{pitch}} + T_{aero}^{pitch}, \end{aligned} \tag{15}$$

where T_{aero}^{flap} and T_{aero}^{pitch} are the flapping aerodynamic torque and the pitching aerodynamic torque, respectively.

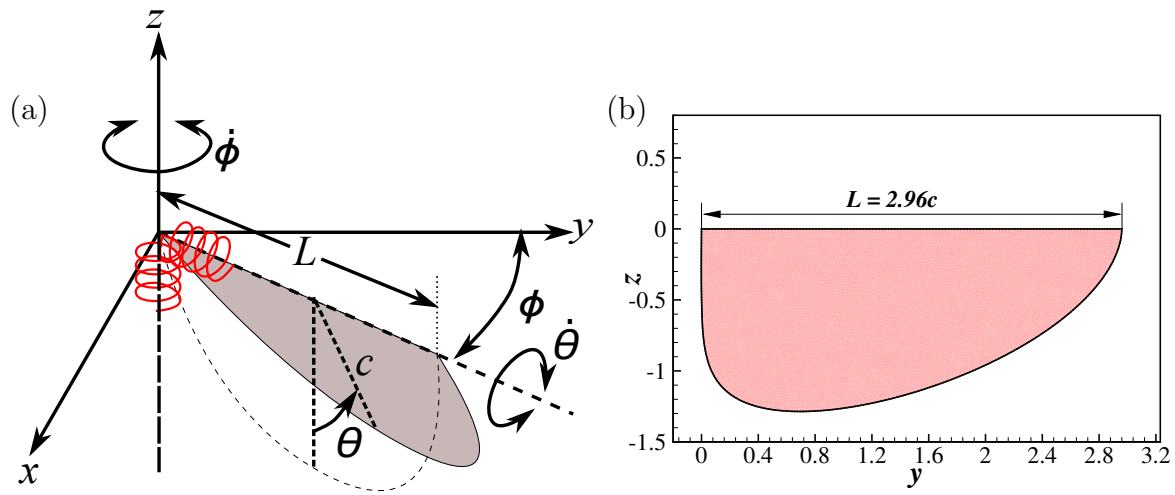

Figure 4: Wing geometry: (a) the schematic shows the two-angle flapping kinematics, with the stroke angle (ϕ) and the pitching angle (θ). $\dot{\phi}$ and $\dot{\theta}$ are the stroke and pitching angular velocity, respectively. c is the mean wing chord, and L is the wingspan. (b) dimensions of the wing planform at $\overline{r}_1 = 0.43$.

1.4 Passively pitching and flapping wing model

In this study, the wing of the mean chord c and span L was modelled to undergo two-angle flapping kinematics, where the two angles of concern are the stroke position angle ϕ and the pitching angle θ, as shown in figure 4. The deviation angle outside the stroke plane was taken as zero as a simplified case of normal hovering. The wing shape was generated using the Beta function ($\beta(p,q)$) by giving the radius of the first moment of area $\overline{r}_1 = 0.43$. The equations for the wing-shape generation were adopted from Ellington (1984),

$$\overline{r}_1 = \int_0^1 \overline{c} \cdot \overline{r} d\overline{r}, \quad \overline{r}_2 = 0.929\,(\overline{r}_1)^{0.732}, \tag{16}$$

$$p = \overline{r}_1 \left(\frac{\overline{r}_1\,(1-\overline{r}_1)}{\overline{r}_2^2 - \overline{r}_1^2} - 1 \right), \quad q = (1-\overline{r}_1) \left(\frac{\overline{r}_1\,(1-\overline{r}_1)}{\overline{r}_2^2 - \overline{r}_1^2} - 1 \right), \tag{17}$$

$$\beta(p,q) = \int_0^1 \overline{r}^{p-1}(1-\overline{r})^{q-1} d\overline{r}, \quad \overline{c} = \frac{\overline{r}^{p-1}(1-\overline{r})^{q-1}}{\beta(p,q)}, \tag{18}$$

where $\overline{c}$ is the wing chord normalised by c and $\overline{r}$ is the spanwise distance from the wing root normalised by L. $\overline{r}_1$ and $\overline{r}_2$ are the non-dimensional radii of the first and second moments of area of the wing, respectively. In our model, the passive flap and pitch dynamics were modelled using torsional springs at the wing hinge. The passive wing stroke dynamics was given as,

$$\underbrace{\left(J_{zz} + J_{yy}\sin^2\theta\right)\ddot{\phi} + J_{yy}\sin(2\theta)\dot{\theta}\dot{\phi} - J_{yz}\left(\ddot{\theta}\cos\theta - \dot{\theta}^2\sin\theta\right)}_{T_{iner}^{flap}} - T_{aero}^{flap} + K_{sf}\phi = \underbrace{-T_A\cos(2\pi f t)}_{T_{\text{Input}}^{flap}}, \tag{19}$$

where J_{zz} is the moment of inertia around the $Z-$axis, J_{yz} is the moment of inertia around $Z-$axis when the wing is rotated around the pitch axis (note, $J_{yz} = J_{zy}$), T_{iner}^{flap} is the flapping

inertial torque, T_{aero}^{flap} is the flapping aerodynamic torque, K_{sf} is the torsional stiffness of the spring for flapping, T_{Input}^{flap} is the total input torque to actuate the wing flap, $T_A = 0.043$ is the input torque amplitude, and f is the input torque frequency. For the passive pitching dynamics, the passive pitching angle θ was determined by solving the dynamical equation for the pitching motion of the wing, as described in Kolomenskiy et al. (2019),

$$\underbrace{-J_{yy}\ddot{\theta} + J_{zy}\ddot{\phi}cos\theta + \frac{1}{2}J_{yy}\dot{\phi}^2 sin2\theta}_{T_{iner}^{pitch}} + T_{aero}^{pitch} - K_{sp}(\theta - \theta_0) - C\dot{\theta} = 0, \tag{20}$$

where J_{yy} is the moment of inertia around the pitching axis, $\ddot{\theta}$ is the pitching angular acceleration, J_{zy} is the moment of inertia around the pitching axis when the wing is rotated around the $Z-$axis (i.e. flapping axis), $\ddot{\phi}$ is the flapping angular acceleration, T_{iner}^{pitch} is the pitching inertial torque, C is the damping coefficient of the spring, K_{sp} is the torsional stiffness of the spring for pitching, $\theta_0 = 0$ is the rest pitching angle, and T_{aero}^{pitch} is the aerodynamic pitching moment on the wing.

The torsional spring stiffness for flapping and pitching were defined using non-dimensional Cauchy numbers (Ch_f and Ch_p),

$$Ch_f = \frac{\rho\phi_A^2 f^2 c^3 L^2}{K_{sf}} = 0.2778 \quad \text{and} \quad Ch_p = \frac{\rho\phi_A^2 f^2 c^3 L^2}{K_{sp}} = 0.2084, \tag{21}$$

where $\phi_A = 165°$ is the peak-to-peak flapping amplitude. The Cauchy numbers provide a relative measure of the aerodynamic forces acting on the wing and the elastic torsional spring force at the wing hinge. The Reynolds number, mass ratio, drag and lift coefficients were defined as

$$Re = \frac{UL}{\nu} = 300, \quad M = \frac{\rho_w h}{\rho c} = 1, \quad CD = \frac{2F_x}{\rho U^2 A}, \quad CL = \frac{2F_z}{\rho U^2 A}, \tag{22}$$

where $U = 2f\phi_A L$ is the mean wingtip velocity, ρ_w is the density of the wing material, and $h = 0.03c$ is the wing thickness. The value of M dictates the relative effects of the aerodynamic forces versus the inertial forces. Here F_x and F_z are the forces acting on the wing by the ambient fluid in the x and z directions, respectively. A is the surface area of the wing.

1.5 Numerical methods

The D3Q19 lattice Boltzmann method (LBM) with multi-relaxation-time (MRT) model was adopted for simulating the flow over a flapping wing. Two-way fluid-structure interactions are coupled by a feedback immersed-boundary method (IBM). The velocity error, streamline penetration and the consequences of the IB-LBM have been discussed in Huang et al. (2022). The numerical method used here has been extensively validated in our previous publications (Huang et al., 2020, 2021b; Huang, 2021; Huang et al., 2021c,a) for various flow conditions. The computational domain has a size of $30c \times 30c \times 30c$. The finest grid around the wing is of size $0.04c$, and the total grid number is 7.25×10^6. The grid size of the wing is half of the finest fluid grid size (i.e. $0.02c$).

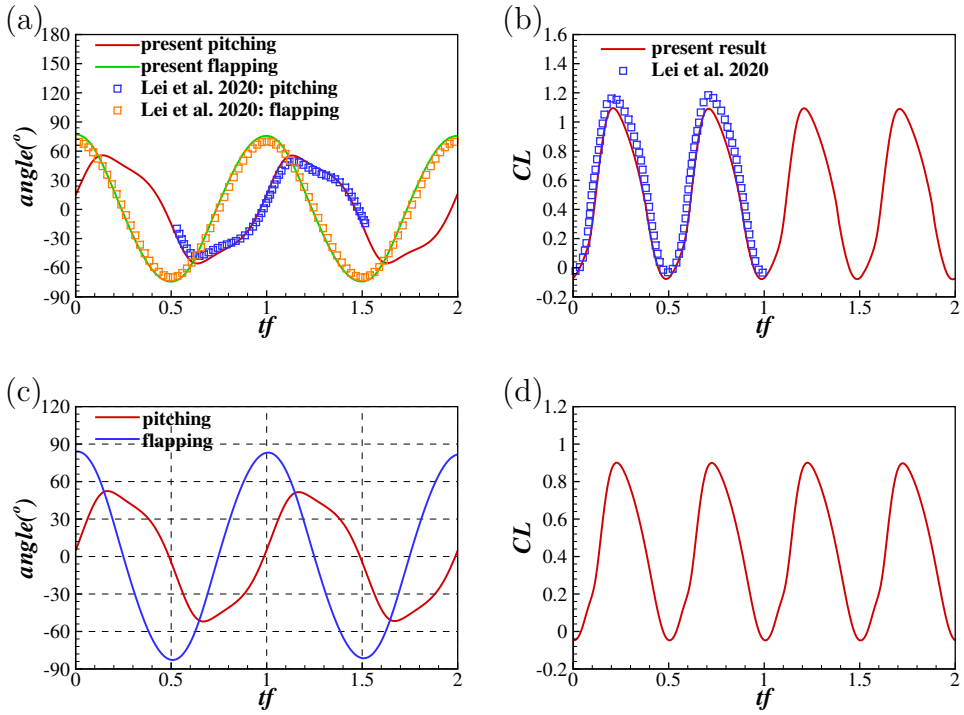

Figure 5: Validation against the prescribed flapping with passive pitching case in Lei and Li (2020): (a) wing kinematics in two stroke cycles; (b) time history of the lift coefficients CL. Simulation results of the passive flapping and pitching model: (c) wing kinematics in two stroke cycles; (d) time history of CL.

1.6 Results

A fruit fly wing in hover with prescribed flapping and passive pitching was performed to validate the proposed two elastic wing-hinge model. In the simulation, ksf was set to 0 in equation 19 to approximate the prescribed flapping motion. The input torque was assumed as cosine waves with amplitude $TA = 0.0018183$ measured from the prescribed flapping simulation. $Re = 300$, $M = 1$, and $Ch_p = 0.15$. More simulation parameters can be found in Lei and Li (2020). Figures 5(a) and 5(b) show the time histories of the pitching angle, flapping angle, and lift coefficient CL, which agree well with the prescribed flapping and passive pitching results of Lei and Li (2020). A passive flapping and pitching wing simulation was performed based on the validated model. The simulation parameter was introduced in Section 1.4. Figure 5(c) shows wing kinematics, where the passive flapping motion profile is a sinusoidal wave and leads the passive pitching motion by a phase of $\sim 50°$. Figure 5(d) shows the time history of CL, where the variation in CL is consistent across two consecutive cycles. Figure 6 shows a clear leading edge vortex (LEV), which is the dominant flow feature responsible for the high lift at $t/T = 5.5$. The LEV creates a high suction pressure on the wing surface beneath the vortex. The LEV is smaller near the root and increases in size in the spanwise direction.

1.7 Conclusions

A fluid-structure interaction model that couples two elastic wing-hinge dynamics and unsteady flapping aerodynamics was proposed to explore passive flapping and pitching mechanisms in a

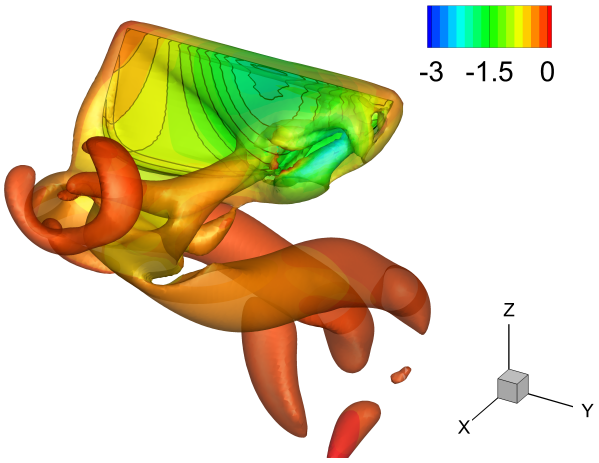

Figure 6: Vortices are visualized by semi-transparent iso-surfaces of the normalised Q-criterion ($Q^* = 50$) and the wing suction sides are coloured by the normalised pressure [$p^* = p/(\rho U^2)$] contours at $t/T = 5.5$.

fruit-fly model, which may improve our understanding of indirect-flight actuation mechanisms of insects. The results provide validation data for benchmarking computational fluid dynamics solvers in the simulation of passively flapping and pitching wings.

2 Dynamic mode decomposition for unsteady flow over flapping wings

2.1 Introduction

Deviation from the steady flow is an expected and routine reality for flapping wings in natural outdoor environments where unsteadiness and/or perturbations are ubiquitous. Freestream perturbations can inflict significant excursion in instantaneous forces and moments over wings and limit the operational domain of crafts. Flapping wings experiencing dynamic stall are particularly vulnerable to perturbations due to the inherently unsteady flow profile present, and the interaction with perturbations results in highly transient and complex dynamics. A long-standing desire to advance the state of airfoil aerodynamics, be it the expansion of the operational envelope or attainment of greater control authority, has ushered in a breadth of work examining dynamic flow separation and the response of such phenomenon to excitation and perturbation (Mueller, 2013).

Various studies have examined the effect of freestream perturbations on airfoils and wings in deep stall by considering archetypal airflow conditions such as von Kármán wakes (Gopalkrishnan et al., 1994) or grid turbulence (Combes and Dudley, 2009), or gust inflow (Mazharmanesh et al., 2021; Poudel et al., 2021). Poudel et al. (2021) numerically studied the effect of vertical gusts on stationary and oscillating rigid NACA0012 airfoil at low Reynolds numbers. They found that increasing the reduced frequency of the oscillating airfoil dominates the gust and results in predictable lift and drag behavior. While previous studies have been mainly focused on the overall performance of airfoils/wing subjected to freestream perturbations, our knowledge of the receptivity of the unsteady flow occurring over dynamically stalling wings to freestream-induced perturbations remains limited. Furthermore, due to the inherently unsteady motion of airfoils/wings during dynamic stall and the vastly varying perturbations encountered, the flowfield is complex and the development of robust control strategies using conventional analytical methods is difficult.

Dynamic Mode Decomposition (DMD) has attracted growing interest in the research community due to recent advancements in generating large experimental and numerical data sets. DMD is a purely data-driven and equation-free technique for reduced-order modelling of dynamical systems and fluid flows (Schmid, 2010, 2021). DMD finds a best fit linear reduced-order model representing any given spatiotemporal data. In DMD, each mode evolves with a fixed frequency, and therefore DMD modes represent physically meaningful structures that are ranked based on their dynamics (Habibi et al., 2020). The inherent property of DMD to isolate transient modes has increased its appeal to study fluid flow phenomena with some impressive results, highlighting its predictive capacity. DMD has also been used in many airfoil studies. For example, Mariappan et al. (2014) applied DMD to investigate the unsteady flowfield around a pitching airfoil under attached flow and dynamic stall conditions at high Reynolds numbers ($960,000 \leq Re \leq 2000,000$). They found that a lower-dimensional representation constructed using the DMD modes is sufficient to capture 85% of the flow field. Mohan and Gaitonde (2017) conducted a DMD analysis of stall control for a rigid NACA0015 airfoil at a Reynold number $Re = 100,000$ and a 15° angle of attack. They found that $St = 2$ for the dominant mode representing stall. They controlled the frequency at $St = 2$ using a nanosecond-pulsed dielectric barrier discharge near the leading edge, and found that the control tends to excite and destabilize predominantly higher frequencies, but it specifically

stabilizes the low-frequency large scale structures associated with the stall. Naderi et al. (2019) showed a combination of the DMD and machine learning algorithms for the modal decomposition of the dynamic stall of a pitching airfoil. Kou and Zhang (2019) proposed DMD with exogenous input approach that takes into account the external input terms to model the pressure field of a flapping NACA0012 airfoil at a high angles of attack 25° and a Reynolds number $Re = 40,000$. Menon and Mittal (2020) applied DMD to flow over sinusoidally pitching, and found that the modes at the oscillation frequency and the first harmonic contain the separating shear layer, and its roll-up into LEV-like structures. There are also many other data-driven approaches for the dynamic stall of airfoils. For example, Wang et al. (2021) successfully predicted unsteady aerodynamics of the dynamic stall based on a data fusion neural network by fusing experimental data and numerical simulations.

Such findings motivate this study to use modal analysis techniques such as DMD to study complex flow separation mechanisms and to facilitate the development of improved aerodynamic models and strategies for disturbance control and mitigation. In addition, identifying modality transformations and operational regimes will foster a fundamental understanding of the coupling of disturbances impinging on dynamic lifting surfaces.

2.2 Methodology

Here an in-house code based on the immersed boundary-lattice Boltzmann method (IB-LBM) (Huang et al., 2020, 2021,c,a,b; Huang, 2021) is used for the flow simulations on dynamically oscillating wings. An in-house MATLAB code of DMD is used to analyze the wake and the unsteady separation of boundary layers at the leading edge. This method takes snapshots of the flow field and computes the modes that govern the dynamics. This framework is used to analyze the key dynamic modes.

2.2.1 Flow simulation

The unsteady incompressible flow is governed by the continuity and Navier-Stokes equations

$$\nabla \cdot \boldsymbol{u} = 0, \quad \frac{\partial \boldsymbol{u}}{\partial t} + \boldsymbol{u} \cdot \nabla \boldsymbol{u} = -\frac{1}{\rho}\nabla p + \nu \nabla^2 \boldsymbol{u} + \boldsymbol{f}, \tag{23}$$

where $\boldsymbol{u}$ is the fluid velocity, ρ is the constant density, $\boldsymbol{f}$ is the body force and p and ν are pressure and kinematic viscosity, respectively.

For simplicity, only the two-dimensional (2-D) numerical method is presented here; the extension to three-dimensions is straightforward. The D2Q9 lattice Boltzmann method (LBM) with multi-relaxation-time (MRT) model is adopted for the fluid dynamics. The lattice arrangement for D2Q9 model is shown in figure 7. The two-way fluid-structure interactions are coupled by an iterative feedback IBM. The details of the method are given in the following subsections. In the LBM, the computational domain is discretised with a fixed Eulerian grid (lattice grid). The fluid is modelled as a set of fictive particles undergoing streaming and collision over a lattice grid. The macroscopic dynamics of the fluid is the result of the statistical behaviour of the particles, which is described by the distribution function $g_i(\boldsymbol{x}, t)$ according to (Lallemand and Luo, 2000; Luo et al., 2011)

$$g_i(\boldsymbol{x} + \boldsymbol{e}_i \Delta t, t + \Delta t) - g_i(\boldsymbol{x}, t) = \Omega_i(\boldsymbol{x}, t) + \Delta t G_i, \tag{24}$$

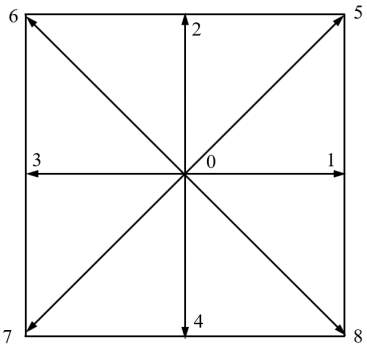

Figure 7: Lattice arrangement for D2Q9 model. "D2" stands for "2 dimensions", while "Q9" stands for "9 particle speeds".

where $g_i(\boldsymbol{x}, t)$ is the distribution function for particles with velocity $\boldsymbol{e}_i$ at position $\boldsymbol{x}$ and time t, Δt is the time increment, $\Omega_i(\boldsymbol{x}, t)$ is the collision operator, and G_i is the forcing term accounting for the body force $\boldsymbol{f}$. The D2Q9 model is used on a square lattice, of which the discrete velocity components can be represented as

$$\begin{aligned}
&\boldsymbol{e_0} = (0, 0), \\
&\boldsymbol{e_i} = (\cos[\pi(i-1)/2], \sin[\pi(i-1)/2])c_\Delta, i = 1-4, \\
&\boldsymbol{e_i} = \sqrt{2}(\cos[\pi(i-9/2)/2], \sin[\pi(i-9/2)/2])c_\Delta, i = 5-8,
\end{aligned} \tag{25}$$

where $c_\Delta = \Delta x/\Delta t$ with Δx the lattice spacing. Compared to the single relaxation time (SRT) collision model, the multiple relaxation time (MRT) model has been proven to be more numerically stable (Lallemand and Luo, 2000). Therefore, the MRT collision model is adopted here and is given by (Lallemand and Luo, 2000),

$$\Omega_i = -(\boldsymbol{M}^{-1}\boldsymbol{S}\boldsymbol{M})_{ij}[g_i(\boldsymbol{x}, t) - g_i^{eq}(\boldsymbol{x}, t)], \tag{26}$$

where $\boldsymbol{M}$ is a 9×9 transform matrix, and $\boldsymbol{S} = diag(\tau_0, \tau_1, \ldots, \tau_8)^{-1}$ is a non-negative diagonal 9×9 relaxation matrix. The determination of $\boldsymbol{S}$ in the two-dimensional (2-D) model can be found in Luo et al. (2011). The equilibrium distribution function g_i^{eq} is defined as

$$g_i^{eq} = \rho\omega_i\Big[1 + \frac{\boldsymbol{e_i}\cdot\boldsymbol{u}}{c_s^2} + \frac{\boldsymbol{uu} : (\boldsymbol{e_i}\boldsymbol{e_i} - c_s^2\boldsymbol{I})}{2c_s^4}\Big], \tag{27}$$

where $c_s = \Delta x/(\sqrt{3}\Delta t)$ is the speed of sound, $\boldsymbol{I}$ is the unit tensor, and the weighting factors ω_i are given by $\omega_0 = 4/9$, $\omega_{1-4} = 1/9$ and $\omega_{5-8} = 1/36$. The mass density ρ, pressure p, and velocity $\boldsymbol{u}$ are respectively calculated by

$$\rho = \sum_i g_i, \quad p = \rho c_s^2, \quad \boldsymbol{u} = \left(\sum_i \mathbf{e}_i g_i + \frac{1}{2}\boldsymbol{f}\Delta t\right) \Big/ \rho. \tag{28}$$

The force scheme proposed by Guo et al. (2002) is adopted to determine G_i,

$$G_i = [\boldsymbol{M}^{-1}(\boldsymbol{I} - \boldsymbol{S}/2)\boldsymbol{M}]_{ij}F_i, \tag{29}$$

$$F_i = \left(1 - \frac{1}{2\tau}\right)\omega_i \left[\frac{\boldsymbol{e}_i - \boldsymbol{u}}{c_s^2} + \frac{\boldsymbol{e}\cdot\boldsymbol{u}}{c_s^4}\boldsymbol{e}_i\right]\cdot \boldsymbol{f}, \tag{30}$$

where τ is the non-dimensional relaxation time.

The two-way interactions between the fluid and the structure are coupled by the feedback law (Kim and Peskin, 2007),

$$\boldsymbol{F}_{ib}(s,t) = \beta\rho(\boldsymbol{x},t)(\boldsymbol{U}_{ib}(s,t) - \boldsymbol{U}(s,t)), \tag{31}$$

where $\boldsymbol{F}_{ib}(s,t)$ is the Lagrangian force density, β is the feedback coefficient and $\beta = 2m/s$ in LBM simulations. In dimensionless form $\beta^* = \beta/U_0 = 40$, and β^* ranges from 20 to 104 (Huang et al., 2021b). $\boldsymbol{U}_{ib}(s,t)$ is the immersed boundary velocity, and $\boldsymbol{U}(s,t)$ represents the velocity of the solid wall, $\boldsymbol{U}(s,t) = 0$ for a rigid solid wall.

A Dirac delta function is used to transfer the interactions between the Lagrangian and Eulerian variables. The velocity interpolation and Lagrangian force distribution to the adjacent Eulerian grid points are calculated according to

$$\boldsymbol{U}_{ib}(s,t) = \int \boldsymbol{u}(x,t)\delta(\boldsymbol{x} - \boldsymbol{X}(s,t))d\boldsymbol{x}, \tag{32}$$

$$\boldsymbol{f}(\boldsymbol{x},t) = -\int \boldsymbol{F}_{ib}(s,t)\delta(\boldsymbol{x} - \boldsymbol{X}(s,t))ds, \tag{33}$$

where $\boldsymbol{u}(x,t)$ is the fluid velocity, $\boldsymbol{x}$ is the coordinate of the fluid lattice nodes, $\delta(\boldsymbol{x} - \boldsymbol{X}(s,t))$ is Dirac delta function, $\boldsymbol{X}$ is the coordinate of the solid wall, $\boldsymbol{f}$ is the body force added in the Navier-Stokes equation to mimic a boundary condition, and ds is the arc length of the immersed boundary.

The 4-point discrete delta function $\delta_h(\boldsymbol{x})$ developed by Peskin (2002) is used to approximate the Dirac delta function,

$$\delta_h(\boldsymbol{x}) = \frac{1}{\Delta x \Delta y}\phi(\frac{x}{\Delta x})\phi(\frac{y}{\Delta y}), \tag{34}$$

$$\phi(r) = \begin{cases} \frac{1}{8}\left(3 - 2|r| + \sqrt{1 + 4|r| - 4r^2}\right), & 0 \le |r| \le 1, \\ \frac{1}{8}\left(5 - 2|r| - \sqrt{-7 + 12|r| - 4r^2}\right), & 1 \le |r| \le 2, \\ 0, & |r| > 2. \end{cases} \tag{35}$$

The IB-LBM FSI solver has high fidelity and compared with the conventional arbitrary Lagrangian-Eulerian (ALE) method, the algorithm is straightforward because a Cartesian mesh is used, and mesh movement is avoided. Further, the advantages of explicit calculation and the intrinsic parallel nature of LBM make the IB-LBM FSI solver much more computationally efficient than the conventional ALE FSI solver.

2.2.2 Dynamic mode decomposition

The DMD used here is a snapshot-based method where the data matrices are organized so that each column provides the system's state at a given instant, and each row contains the time history of a specific state variable. In the IB-LBM simulation framework, the calculated fluid data of each snapshot is given on a stationary Cartesian grid. The flow field in each snapshot is represented as state vector $\mathbf{x_k}$, which is made up of $nx \times ny$ grid points and flow variables

of interest at every grid point. The index k denotes the snapshot at the kth time step. The snapshot of the flow field is sampled at a time interval of Δt. The number of snapshots used in the DMD is N, and these snapshots are synthesized into a data matrix $\mathbf{X}$:

$$\mathbf{X} = [\mathbf{x}_1, \mathbf{x}_2, \ldots, \mathbf{x}_N] \tag{36}$$

An additional snapshot matrix $\mathbf{X}'$ is collected by shifting the data matrix $\mathbf{X}$ by one time step:

$$\mathbf{X}' = [\mathbf{x}_2, \mathbf{x}_3, \ldots, \mathbf{x}_{N+1}] \tag{37}$$

The idea of the DMD is to approximate the evolution of observable vectors (e.g. velocity or vorticity) from the one time step to the next by a high-dimensional linear approximation:

$$\mathbf{x}_{k+1} = \mathbf{A}\mathbf{x}_k \tag{38}$$

where $\mathbf{A}$ is a large system matrix that governs this evolution. The matrix $\mathbf{A}$ should satisfy min $\sum_{k=1}^{N-1} \|\mathbf{x}_{k+1} - \mathbf{A}\mathbf{x}_k\|_2$ to best maps the progress of the state from one time step to the next. The solution to the system is expressed simply in terms of the eigenvalues λ_k and eigenvectors ϕ_k of the system matrix $\mathbf{A}$:

$$\mathbf{x}_k = \sum_{j=1}^{r} \boldsymbol{\phi}_j \lambda_j^k b_j = \boldsymbol{\Phi}\boldsymbol{\Lambda}^k \mathbf{b}, \tag{39}$$

where r is the truncated order, and $\mathbf{b}$ are the coefficients of the initial condition $\mathbf{x}_1$ in the eigenvector basis, so that $\mathbf{x}_1 = \boldsymbol{\Phi}\mathbf{b}$. The DMD algorithm is summarized as below.

1. Approximate map:
$$\mathbf{X}' \approx \mathbf{A}\mathbf{X} \tag{40}$$

2. Take the singular value decomposition (SVD) of $\mathbf{X}$:
$$\mathbf{X} \approx \mathbf{U}\boldsymbol{\Sigma}\mathbf{V}^* \tag{41}$$

3. Reduced matrix: the matrix $\mathbf{A}$ is obtained by using the pseudoinverse of $\mathbf{X}$ obtained via the SVD:
$$\mathbf{A} = \mathbf{X}'\mathbf{V}\boldsymbol{\Sigma}^{-1}\mathbf{U}^* \tag{42}$$
In practice, the matrix $\mathbf{A}$ may be intractable to analyze directly when the state dimension is large. Instead, DMD implements the eigendecomposition of $\tilde{\mathbf{A}}$ which is a rank-reduced representation of the matrix $\mathbf{A}$ by applying $r \times r$ projection of the $\mathbf{A}$ onto proper orthogonal decomposition (POD) modes:
$$\tilde{\mathbf{A}} = \mathbf{U}^*\mathbf{A}\mathbf{U} = \mathbf{U}^*\mathbf{X}'\mathbf{V}\boldsymbol{\Sigma}^{-1} \tag{43}$$

4. Compute the eigendecomposition of $\tilde{\mathbf{A}}$:
$$\tilde{\mathbf{A}}\mathbf{W} = \mathbf{W}\boldsymbol{\Lambda}, \tag{44}$$
where columns of $\mathbf{W}$ are eigenvectors and $\boldsymbol{\Lambda}$ is a diagonal matrix containing the corresponding eigenvalues λ_k.

5. Compute modes: reconstruct the eigendecomposition of $\mathbf{A}$ from $\mathbf{W}$ and $\mathbf{\Lambda}$. The eigenvalues of $\mathbf{A}$ are given by $\mathbf{\Lambda}$ and the eigenvectors of $\mathbf{A}$ (i.e. DMD modes) are given by columns of $\mathbf{\Phi}$:

$$\Phi = \mathbf{X'V\Sigma}^{-1}\mathbf{W}. \tag{45}$$

6. Construct the projected solution for all time in the future with the low-rank approximations of both the eigenvalues and the eigenvectors. The approximate solution at all future time is approximated as

$$\mathbf{x}(t) \approx \sum_{k=1}^{r} \phi_k \exp\left(\omega_k t\right) b_k = \mathbf{\Phi} \exp(\mathbf{\Omega} t)\mathbf{b} \tag{46}$$

where $\omega_k = \ln\left(\lambda_k\right)/\Delta t$, b_k is the initial amplitude of each mode, $\mathbf{\Phi}$ is the matrix whose columns are the DMD eigenvectors ϕ_k, and $\mathbf{\Omega} = diag(\omega)$ is a diagonal matrix whose entries are the eigenvalues ω_k.

Here the eigenvalues ω_k is a complex number whose real and imaginary parts give the growth rate and frequency, respectively, of mode k. The resulting DMD modes are ranked according to an efficient and robust criterion that considers both accuracy and modal energy (Kou and Zhang, 2017), through integrating the time evolution of mode coefficients (absolute value) in the sampling space.

2.3 Preliminary Results

2.3.1 2-D NACA0015 flapping foil

Here the simulation of a 2-D rigid NACA0015 foil in a uniform flow is conducted to validate the IB-LBM solver. The foil is pivoted at a point located on the chord line at $1/3c$ from the leading edge, where c is the chord length. The pitching and plunging motions of the foil are described as

$$\theta(t) = \theta_0 \cos(2\pi f t), \tag{47}$$

$$h(t) = h_0 \cos(2\pi f t + \phi), \tag{48}$$

where $\theta_0 = 76.3^o$ is the pitching amplitude, h is the vertical displacement, $h_0 = c$ is the heaving amplitude, and $\phi = 90^o$ is the phase angle between the two motions. The non-dimensional flapping frequency $fc/U_0 = 0.14$. The Reynolds number $Re = U_0 c/\nu = 1100$, where U_0 is the free-stream velocity. The computational domain is $40c \times 30c$ with the minimum grid size of $0.00625c$.

Grid distribution and vorticity contours are shown in figure 8. The grid is dynamically refined and coarsened according to the movement of the foil. The structures of the leading and trailing edge vortices are well captured. Figure 9 shows the time histories of the drag and lift coefficients, which agree well with the computational result of Kinsey and Dumas (2008) and Tian et al. (2015).

2.3.2 DMD for flow over a stationary cylinder

Here the DMD code is tested for flow over a stationary cylinder at Reynolds number $Re = DU_0/\nu = 100$, where D is the cylinder diameter, and U_0 is the free-stream velocity. At $Re =$

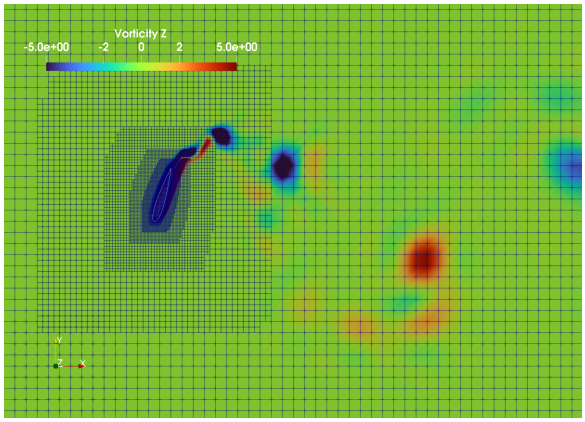

Figure 8: Z-vorticity contours of a NACA0015 flapping foil at $t/T = 8.6$.

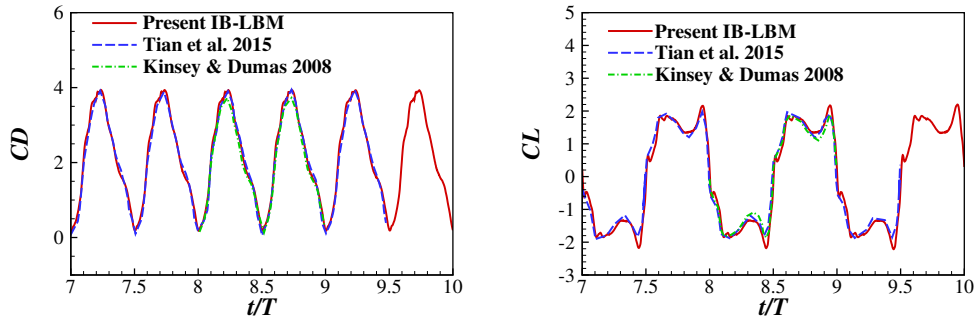

(a) C_D; (b) C_L.

Figure 9: Comparison of drag and lift coefficients time histories for a NACA0015 flapping foil at $Re = 1100$.

100 the cylinder wake is in a periodic vortex shedding flow regime. Figure 10 shows a schematic depiction of the flow over the cylinder with boundary conditions and dimensions used. The computational domain is a rectangular box ($x \in [-15D, 25D]$ and $y \in [-10D, 10D]$). The finest domain is of size $x \in [-1D, 8D]$ and $y \in [-2D, 2D]$, and the grid size for the fluid and the cylinder is $0.02D$ and $0.01D$, respectively. The cylinder is placed in the domain with its centre located at the origin (i.e. $(x, y) = (0, 0)$). A uniform velocity profile U_0 and a constant pressure P_0 are imposed at the inlet. No-slip walls are enforced at the wall of the cylinder. A slip boundary condition is imposed at the top and bottom sides of the computational domain. The normal and shear stress are set to zero at the outlet.

Figure 11(a) shows the time history of the lift coefficient from the simulation. The DMD analysis is performed after transients are no longer present and the system has attained periodic behaviour of fixed amplitude and frequency of the lift coefficient. The snapshots are output from the simulation over the range $t/T \in [80, 120]$ (shaded in figure 11(a)) with sampling interval $\Delta t_s/T = 0.1$. $T = D/U_0$ is the reference time. The non-dimensional time step in the simulation is $\Delta t/T = 0.004$. As shown in figure 11(a), seven periods of vortex shedding are sampled. Figure 11(b) shows the Ritz values computed from the DMD, where all modes lie on the unit circle, indicating that the corresponding modes are neither growth nor decay.

Figure 12 shows the vorticity for modes 1 to 6. Mode 1 represents the mean flow with the

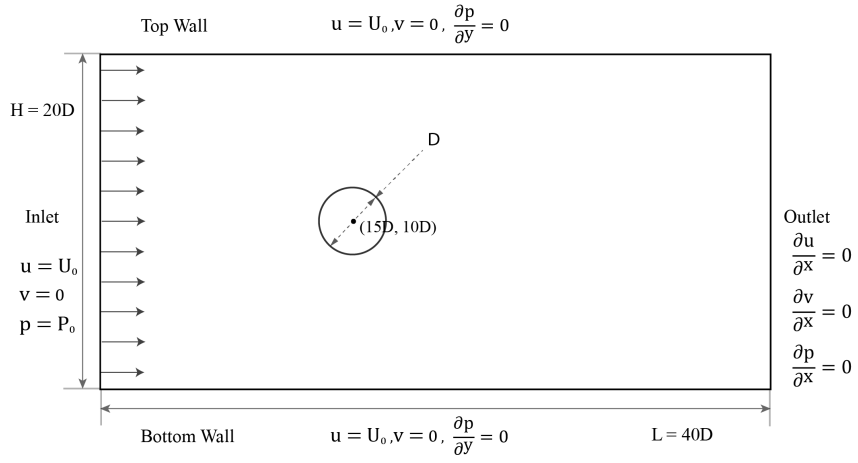

Figure 10: Schematic diagram of flow over a stationary cylinder.

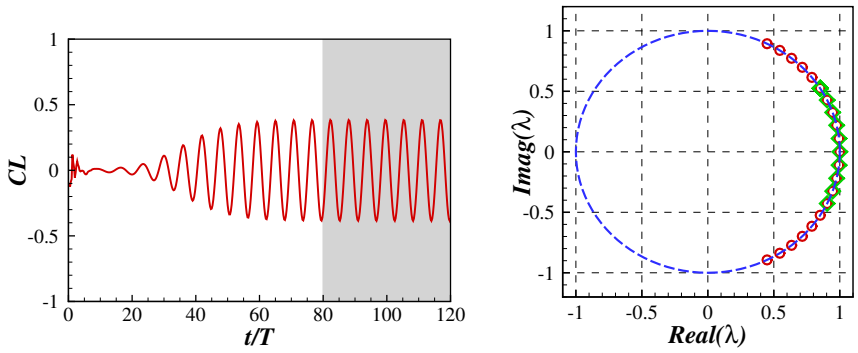

(a) CL; (b) Ritz values.

Figure 11: Flow over a stationary cylinder at $Re = 100$: (a) lift coefficients; (b) Ritz values computed from the DMD. $T = D/U_0$ is the reference time.

typical shear layers developing from the top and bottom of the cylinder. Mode 2, 4 and 6 show symmetric patterns around the horizontal centre-line, corresponding to the convection of the large scale structures downstream of the cylinder. Mode 3 and 5 show anti-symmetric patterns, corresponding to the shedding of the vortices in the wake of the cylinder. All these observations are in agreement with the results of Chen et al. (2012).

Table 1: Strouhal number (St) and growth rate (GR) of each mode. In the numerical simulation, the Strouhal number is $St = 0.1786$.

Modes	1	2	3	4	5	6
St	0	0.1758	0.3516	0.5274	0.879	1.0548
GR	0	0	0	0	0	0

Table 1 shows the Strouhal number St and growth rate GR of each mode. $St = 0.1786$ in the numerical simulation. Mode 2 has $St = 0.1758$, which contains the base frequency of the flow. For modes 3, 4, 5 and 6, the oscillatory mode frequencies are nearly integral multiples of

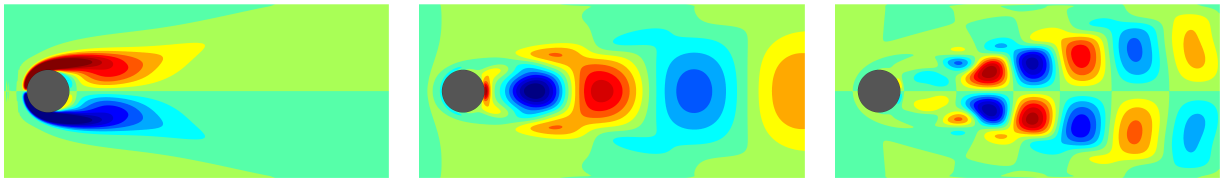

(a) mode 1; (b) mode 2; (c) mode 3;

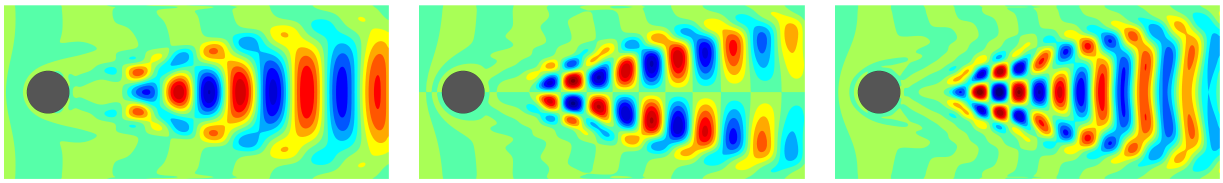

(d) mode 4; (e) mode 5; (f) mode 6.

Figure 12: Dynamic mode decomposition of flow over a stationary cylinder at $Re = 100$. The vorticity ranges from -0.01 (blue) to 0.01 (red). The vorticity is non-dimensionalized by U_0/D.

the base frequency $St = 0.1758$. The integral multiples suggest that the periodic flow of the cylinder exhibits harmonic-like behavior.

2.4 Conclusion

Validations of an in-house IB-LBM FSI solver for the computations of the pitching and plunging motions of a 2-D NACA0015 foil in uniform flow is performed. Good agreement of results between current computations and published data was observed, suggesting the present FSI solver can accurately compute the flow over flapping wing systems. The modes computed by present DMD codes agree well with previously published data. The effects of the freestream perturbations will be reported in future works.

References

Bergou, A.J., Xu, S., Wang, Z.J., 2007. Passive wing pitch reversal in insect flight. J. Fluid Mech. 591, 321–337.

Chen, K.K., Tu, J.H., Rowley, C.W., 2012. Variants of dynamic mode decomposition: boundary condition, koopman, and fourier analyses. Journal of Nonlinear Science 22, 887–915.

Chen, Y., Gravish, N., Desbiens, A.L., Malka, R., Wood, R.J., 2016. Experimental and computational studies of the aerodynamic performance of a flapping and passively rotating insect wing. J. Fluid Mech. 791, 1–33.

Chen, Y., Zhao, H., Mao, J., Chirarattananon, P., Helbling, E.F., Hyun, N.s.P., Clarke, D.R., Wood, R.J., 2019. Controlled flight of a microrobot powered by soft artificial muscles. Nature 575, 324–329.

Combes, S.A., Dudley, R., 2009. Turbulence-driven instabilities limit insect flight performance. Proceedings of the National Academy of Sciences 106, 9105–9108.

Eldredge, J.D., Jones, A.R., 2019. Leading-edge vortices: mechanics and modeling. Annu. Rev. Fluid Mech. , 75–104.

Ellington, C.P., 1984. The aerodynamics of hovering insect flight. I. The quasi-steady analysis. Philos. Trans. R. Soc. Lond., B, Biol. Sci. 305, 1–15.

Ennos, A.R., 1988. The inertial cause of wing rotation in diptera. J. Exp. Biol. 140, 161–169.

Gopalkrishnan, R., Triantafyllou, M.S., Triantafyllou, G.S., Barrett, D., 1994. Active vorticity control in a shear flow using a flapping foil. Journal of Fluid Mechanics 274, 1–21.

Guo, Z.L., Zheng, C.G., Shi, B.C., 2002. Non-equilibrium extrapolation method for velocity and pressure boundary conditions in the lattice Boltzmann method. Chinese physics 11, 366–374.

Habibi, M., Dawson, S., Arzani, A., 2020. Data-driven pulsatile blood flow physics with dynamic mode decomposition. Fluids 5, 111.

Huang, Q., 2021. Low Reynolds number turbulent FSI and its applications in biological flows. Ph.D. thesis. University of New South Wales.

Huang, Q., Bhat, S.S., Yeo, E.C., Tian, F.B., Young, J., Lai, J.C.S., Ravi, S., 2023. Effects of wing shape and hinge properties on the hovering performance of passively pitching flapping wings. J. Fluids Struct (submitted) .

Huang, Q., Liu, Z., Wang, L., Ravi, S., Young, J., Lai, J.C.S., Tian, F.B., 2022. Streamline penetration, velocity error and consequences of the feedback immersed boundary method. Phys. Fluids 34, 097101.

Huang, Q., Mazharmanesh, S., Tian, F.B., Young, J., Lai, J.C.S., Ravi, S., 2021a. CFD solver validations for simulating passively pitching tandem wings in hovering flight, in: MODSIM2021, pp. 71–77.

Huang, Q., Tian, F.B., Young, J., Lai, J.C.S., 2020. A diffused interface immersed boundary–lattice Boltzmann method for simulation of channel flow. AFMC2020, 7-10 December 2020, Brisbane, Australia .

Huang, Q., Tian, F.B., Young, J., Lai, J.C.S., 2021b. Transition to chaos in a two-sided collapsible channel flow. J. Fluid Mech. 926.

Huang, Q., Wang, L., Ravi, S., Tian, F.B., Young, J., Lai, J.C.S., 2021c. Benchmarking a coupled finite element–immersed boundary–lattice Boltzmann method solver for simulations of collapsible tube flows, in: ACCM2021, p. 15.

Huang, Q., Wang, L., Tian, F.B., Young, J., Lai, J.C.S., 2021. A diffused interface immersed boundary–lattice Boltzmann method for simulation of stenosis. 14th WCCM & ECCOMAS Congress .

Kim, Y., Peskin, C.S., 2007. Penalty immersed boundary method for an elastic boundary with mass. Physics of Fluids 19, 053103.

Kinsey, T., Dumas, G., 2008. Parametric study of an oscillating airfoil in a power-extraction regime. AIAA Journal 46, 1318–1330.

Kolomenskiy, D., Ravi, S., Xu, R., Ueyama, K., Jakobi, T., Engels, T., Nakata, T., Sesterhenn, J., Schneider, K., Onishi, R., et al., 2019. The dynamics of passive feathering rotation in hovering flight of bumblebees. J. Fluids Struct. 91, 102628.

Kou, J., Zhang, W., 2017. An improved criterion to select dominant modes from dynamic mode decomposition. European Journal of Mechanics-B/Fluids 62, 109–129.

Kou, J., Zhang, W., 2019. Dynamic mode decomposition with exogenous input for data-driven modeling of unsteady flows. Physics of fluids 31, 057106.

Lallemand, P., Luo, L.S., 2000. Theory of the lattice Boltzmann method: Dispersion, dissipation, isotropy, Galilean invariance, and stability. Physical Review E - Statistical Physics, Plasmas, Fluids, and Related Interdisciplinary Topics 61, 6546–6562.

Lei, M., Li, C., 2020. The aerodynamic performance of passive wing pitch in hovering flight. Phys. Fluids 32, 051902. doi:10.1063/5.0006902.

Luo, L.S., Liao, W., Chen, X., Peng, Y., Zhang, W., 2011. Numerics of the lattice Boltzmann method: Effects of collision models on the lattice Boltzmann simulations. Physical Review E 83, 1–24.

Lynch, J., Gau, J., Sponberg, S., Gravish, N., 2021. Dimensional analysis of spring-wing systems reveals performance metrics for resonant flapping-wing flight. J. R. Soc. Interface 18, 20200888.

Mariappan, S., Gardner, A.D., Richter, K., Raffel, M., 2014. Analysis of dynamic stall using dynamic mode decomposition technique. AIAA journal 52, 2427–2439.

Mazharmanesh, S., Stallard, J., Medina, A., Fisher, A., Ando, N., Tian, F.B., Young, J., Ravi, S., 2021. Effects of uniform vertical inflow perturbations on the performance of flapping wings. Royal Society Open Science 8, 210471.

Menon, K., Mittal, R., 2020. Dynamic mode decomposition based analysis of flow over a sinusoidally pitching airfoil. Journal of Fluids and Structures 94, 102886.

Mohan, A.T., Gaitonde, D.V., 2017. Analysis of airfoil stall control using dynamic mode decomposition. Journal of Aircraft 54, 1508–1520.

Mueller, T.J., 2013. Low Reynolds Number Aerodynamics: Proceedings of the Conference Notre Dame, Indiana, USA, 5–7 June 1989. volume 54. Springer Science & Business Media.

Naderi, M.H., Eivazi, H., Esfahanian, V., 2019. New method for dynamic mode decomposition of flows over moving structures based on machine learning (hybrid dynamic mode decomposition). Physics of Fluids 31, 127102.

Peskin, C.S., 2002. The immersed boundary method. Acta Numerica 11, 479–517.

Poudel, N., Yu, M., Hrynuk, J.T., 2021. Gust mitigation with an oscillating airfoil at low reynolds number. Physics of Fluids 33, 101905.

Schmid, P.J., 2010. Dynamic mode decomposition of numerical and experimental data. Journal of Fluid Mechanics 656, 5–28.

Schmid, P.J., 2021. Dynamic mode decomposition and its variants. Annual Review of Fluid Mechanics 54.

Shyy, W., Kang, C.k., Chirarattananon, P., Ravi, S., Liu, H., 2016. Aerodynamics, sensing and control of insect-scale flapping-wing flight. Proc. R. Soc. A: Math. Phys. Eng. Sci. 472, 20150712.

Spagnolie, S.E., Moret, L., Shelley, M.J., Zhang, J., 2010. Surprising behaviors in flapping locomotion with passive pitching. Phys. Fluids 22, 041903.

Tian, F.B., Wang, Y., Young, J., Lai, J.C., 2015. An FSI solution technique based on the DSD/SST method and its applications. Mathematical Models and Methods in Applied Sciences 25, 2257–2285.

Wang, X., Kou, J., Zhang, W., 2021. A new dynamic stall prediction framework based on symbiosis of experimental and simulation data. Physics of Fluids 33, 127119.

Whitney, J.P., Wood, R.J., 2010. Aeromechanics of passive rotation in flapping flight. J. Fluid Mech. 660, 197–220.

3 Performance Metric

3.1 Peer-reviewed Journal and Conference Papers

1. Huang, Q., Tian, F.-B., Young, J., Lai, J.C.S. and Ravi, S. (2022) Numerical modelling of under-actuated flapping wings inspired by the indirect-flight muscles of insects. 23rd Australasian Fluid Mechanics Conference.

2. Huang, Q., Bhat, S. S., Yeo, E. C., Young, J., Lai, J. C., Tian, F. B., and Ravi, S. (2023). Power synchronisations determine the hovering flight efficiency of passively pitching flapping wings. Journal of Fluid Mechanics, 974, A41.

3. Huang, Q., Kou, J., Tian, F.-B., Young, J., Lai, J.C.S. and Ravi, S. (2023) Dynamic mode decomposition for unsteady flow over flapping wings. In AIAA SCITECH 2023 Forum (p. 1618).